accretion disk (Halpern et al. 2013) and an X-ray luminosity comparable to the known quiescent LMXBs (Coti Zelati et al. 2014).

Here we present *XMM-Newton* observations which show that PSR J1023+0038 intermittently produces coherent, apparently accretion-induced X-ray pulsations during its LMXB state. In Section 2 we present the observations and data analysis. The results are presented in Section 3, and these are discussed in Section 4.

2. OBSERVATIONS AND ANALYSIS

Motivated by this remarkable state change, we observed PSR J1023+0038 with the *X-ray Multi-Mirror-Newton* telescope. Specifically, PSR J1023+0038 was observed with *XMM-Newton* on two separate occasions: starting on 2013 November 10 for 134 kiloseconds (Observation ID 0720030101) and again on 2014 June 10 for 115 kiloseconds (0742610101). For both observations, the European Photon Imaging Camera (EPIC) pn detector was used in fast timing mode, which permits a 30 μs time resolution but at the expense of one imaging dimension, which is used for fast read-out. Both EPIC MOS cameras were employed in small window mode to minimize the deleterious effect of photon pile-up. For all three detectors, the thin optical blocking filter was in place.

The data reduction and extraction were performed with the Science Analysis Software (SAS[9]) version `xmmsas_20130501_1901-13.0.0`. The EPIC events were filtered using the recommended flag and pattern values.

The source events from the EPIC pn fast timing data were extracted using a region of half-width 6.5 pixels in the imaging (RAWX) direction centered on row 37. This translates to an angular size of 27″, which encircles ∼87% of the energy from the point source at 1.5 keV. The MOS1/2 source events were obtained from circular regions of radius 36″, which enclose ∼88% of the total point source energy at 1.5 keV. For the variability analysis and pulsation searches, the photon arrival times were translated to the solar system barycenter using the DE405 solar system ephemeris and the pulsar position with right ascension 10:23:47.687198 and declination +00:38:40.84551 calculated from the astrometric solution given in Deller et al. (2012).

The individual binned, background-subtracted, exposure-corrected light curves for the MOS1/2 and PN were extracted using the SAS command `epiclccorr`. The total EPIC light curve was then obtained by summing the three light curves during the periods when all three telescopes acquired data simultaneously. Both the 2013 November and 2014 June data exhibit multiple instances of enhanced background due to soft proton flares. Since PSR J1023+0038 is on average relatively bright in its accreting state, the intervals of high background were not discarded. Instead the flares were removed in the background subtraction. Comparison between the final source light curve and the background light curve revealed that the background flares were no longer present in the data. This indicates that any remaining bright flares are not due to background but are intrinsic to the source. For the fast timing photon lists, we determined time ranges corresponding to soft proton flares by thresholding a 10-s binned light curve extracted from an off-source region; photons arriving during these time ranges were not used in pulsed flux and profile calculations.

PSR J1023+0038 has a precisely known rotational ephemeris, which predicts the pulsar's rotational phase (Archibald et al. 2013). However, the pulsar exhibits non-deterministic orbital period variations (Archibald et al. 2013). We therefore computed photon arrival phases for a sequence of ephemerides, each constructed from the last known radio ephemeris by varying time of the ascending node ($T_{\rm asc}$) within a range of ±20 s in steps of 0.1 s, and then applied the H test (de Jager et al. 1989) to each set of phases. We searched in the pulsar's spin period as well, but obtained only marginal improvements in detection significance. Uncertainties in the relative timing aboard *XMM-Newton* (Martin-Carrillo et al. 2012) make it impossible to provide physically interesting constraints on the spin period using the existing data.

Further results from these X-ray observations, combined with other multiwavelength data, will be presented in (Bogdanov et al. 2014). There we also describe in detail the spectral fitting and flux calculations. Briefly, we classified the photons based on luminosity mode (see section 3) and carried out spectral fitting in each mode and for each of our two epochs. We found very similar results in the two epochs, and all three modes were adequately fit with power laws (although there is some evidence for a more complicated spectrum in the high mode) with interstellar absorption (N_H) of $3.1(2) \times 10^{-20}\,{\rm cm}^{-2}$. For the low, high, and flare modes in the 2013 November epoch we found photon indices of 1.82(3), 1.71(1), and 1.66(2), respectively; the three modes differ chiefly in their luminosities L_X, which are $5.4(1) \times 10^{32}$, $3.17(2) \times 10^{33}$, and $1.09(2) \times 10^{34}\,{\rm erg\,s}^{-1}$ respectively. For the 2014 June epoch, the photon indices were 1.80(4), 1.75(1), and 1.74(2), while the luminosities were $4.6(1) \times 10^{32}$, $3.06(2) \times 10^{33}$, and $9.6(1) \times 10^{33}\,{\rm erg\,s}^{-1}$ respectively.

The above luminosities are computed for the 0.3–10 keV energy range observed with *XMM-Newton*. For theoretical purposes it would be valuable to estimate the bolometric luminosity of PSR J1023+0038, at least in its high mode. Given the power-law models we obtain from spectral fitting, one must assume spectral cutoffs to obtain a finite bolometric luminosity. Unfortunately no such cutoffs have been observed. Hard X-ray observations with NuSTAR show there is no cutoff below 79 keV, and γ-ray observations with Fermi show there must be a break of some kind below about 100 MeV (Tendulkar et al. 2014). Assuming that the power law begins in the optical and ends somewhere between these two, we compute a range of possible bolometric luminosities in the high mode, from 1.4×10^{34} to $1.1 \times 10^{35}\,{\rm erg\,s}^{-1}$. It may be possible to narrow this range somewhat by using the companion as a bolometer. Thorstensen & Armstrong (2005) studied the companion irradiation in the MSP state and found that the amount of heating seen then was consistent with a 2 $L_\odot$ isotropic irradiation flux. In the accretion-disk state, the companion heating is presumably due to the emission from the disk and pulsar. The light curves in Coti Zelati et al. (2014) give us a measurement of the companion brightness (plus a con-

[9] The *XMM-Newton* SAS is developed and maintained by the Science Operations Centre at the European Space Astronomy Centre and the Survey Science Centre at the University of Leicester.

stant contribution from the disk). If we treat the V and g filters as roughly equivalent, assume that the dark side of the companion has not brightened, and assume that the companion's total brightness is proportional to the flux in these filters, then we find that the companion's bright-side heating has increased by a factor of ∼3. This corresponds to a bolometric luminosity from the accretion disk and pulsar of $\sim 2 \times 10^{34}$ erg s^{-1}, placing it towards the lower end of the above range. Given the very considerable uncertainty in the bolometric luminosity of J1023, in Section 4 we will compare X-ray luminosities (rather than bolometric) to other sources where possible (for example, in Figure 5).

We also observed PSR J1023+0038 with the Karl G. Jansky Very Large Array (VLA) a total of 13 times under the project codes 13B-439 and 13B-445, at frequencies ranging from 1 to 18 GHz. A standard phase referencing setup (using the calibrator source J1024−0052) was used for all observations, and data reduction was performed with the standard VLA pipeline in the Common Astronomy Software Applications (CASA; McMullin et al. 2007) package. PSR J1023+0038 was detected in all epochs except one, appearing as an unresolved, variable, flat-spectrum ($-0.5 \lesssim \alpha \lesssim 0.5$, where luminosity $\propto \nu^{\alpha}$) source. Along with the flat radio spectrum, the rapid variability observed (factor-of-ten change in flux density in 30 minutes) is indicative of outflowing material; similarly variable, flat-spectrum emission in other LMXB systems is attributed to a partially self-absorbed synchrotron emission from a compact jet (for example Migliari & Fender 2006). Further results from these radio observations will be presented in (Deller et al. 2014).

3. RESULTS

A primary goal of our observations was to search for coherent X-ray pulsations. The pulsar's orbital period variations made it necessary to search a modest number of possible orbital phase shifts (in the form of changes of $T_{\rm asc}$) for each observation. At the best values of $T_{\rm asc}$ for our two observing epochs, the (single-trial) false positive probability for each was less than 10^{-500} (∼33σ), indicating a statistically unambiguous detection of pulsations in each observation. The changes in $T_{\rm asc}$ we obtained are large but not unreasonable compared to those observed while the pulsar is in its RMSP state (see Figure 1).

We obtained the pulse profile shapes in our two observations and found them remarkably similar (Figure 2) but subtly different from (as well as much brighter than) the X-ray pulse profile seen in the source's previous RMSP state, where the pulsations are thought to be due to return current heating of the magnetic poles (Archibald et al. 2010) rather than heating by channeled accretion.

Examination of the combined *XMM-Newton* light curves revealed three distinct luminosity modes[10] (Figures 3, A1 and A2), all of which are present during the LMXB state. Similar behavior is seen from PSR J1023+0038 at the higher energies observed with *NuSTAR* (Tendulkar et al. 2014), as well as during the

[10] The PSR J1023+0038 system has been observed to switch between RMSP and LMXB *states*. To describe the different X-ray luminosities observed during the LMXB state, we use the term *mode*, that is, low, high and flare mode.

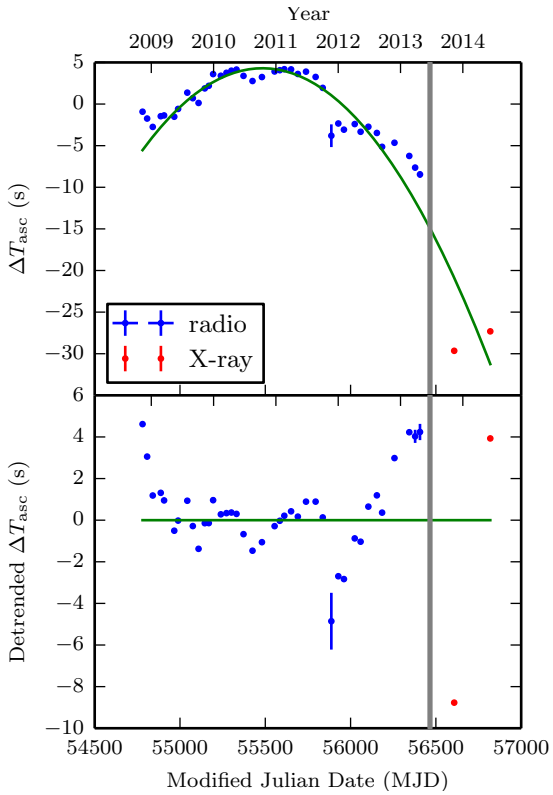

Figure 1. Variations in the time of the ascending node of the binary orbit, $T_{\rm asc}$. Blue points are measurements made by Archibald et al. (2013) based on radio timing; horizontal bars indicate the span of time over which the orbit was fit, and vertical bars reflect an uncertainty in the fitted values that includes unmodelled orbital deviations. The green curve is a best-fit parabola through these blue points, reflecting a long-term average binary period and binary period derivative. The gray vertical bar indicates when the radio disappearance occurred (Stappers et al. 2014). The red points are obtained from the two *XMM-Newton* observations presented here by optimizing the detection significance; their uncertainties are too small to see on this scale. The top panel was computed using a constant binary period of 0.198096315 day, obtained from long-term radio timing (Archibald et al. 2013). The bottom panel shows the residuals after subtraction of the green parabola, corresponding to a steady orbital period derivative of -9.05×10^{-12}.

LMXB states of the two other known transitional RMSPs: PSR J1824−2452I and XSS J12270−4859 (Linares et al. 2014; de Martino et al. 2013; Linares 2014). In the 0.3–10 keV photon energy range, our *XMM-Newton* observations show a steady 'low' mode with luminosity $\sim 5 \times 10^{32}\,{\rm erg\,s^{-1}}$, a steady 'high' mode with luminosity $\sim 3 \times 10^{33}\,{\rm erg\,s^{-1}}$, and occasional, more erratic 'flares' during which the luminosity typically exceeds $5 \times 10^{33}\,{\rm erg\,s^{-1}}$, and reaches as high as $3 \times 10^{34}\,{\rm erg\,s^{-1}}$. The three modes have similar hard power-law spectra (photon index ∼1.7; Tendulkar et al. 2014). The low, high, and flare modes occupy roughly 20%, 80%, and 1–2% of the data, respectively, in both the 2013 November and 2014 June data sets. Switching between the low and high modes appears to occur within $10 - 30\,{\rm s}$, while the flares have a more complex structure. The low and high mode durations are typically tens of seconds up to tens of minutes long, and the distribution of their durations follows a power law (Tendulkar et al. 2014). No obvious periodicity or other discernible regular pattern is present. Moreover, the luminosity in low/high mode appears to be nearly constant and equal in both the 2013 November

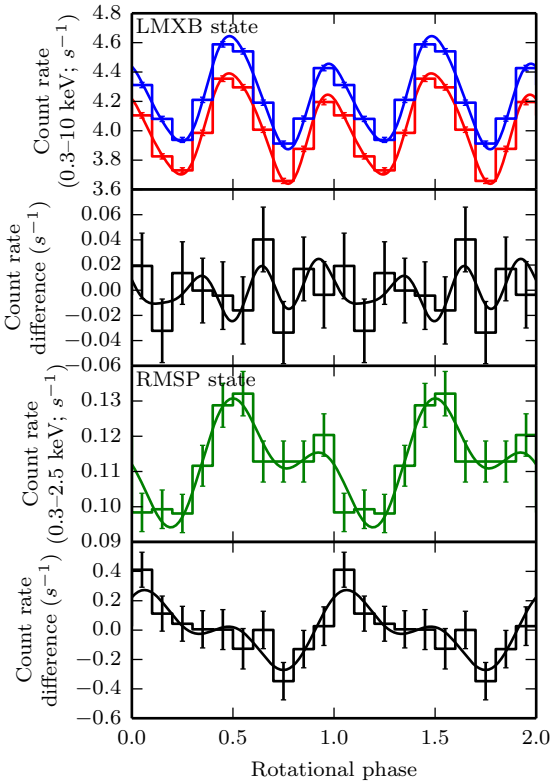

Figure 2. Top panel: the LMXB-state pulse profiles computed from the 2013 November (blue, top) and 2014 June (red, bottom) observations, when the radio pulsar was unobservable. Two rotational cycles are shown for clarity, with both a histogram and a multiple-sinusoid representation (see appendix for details). The 2014 November observation has rms amplitude $0.236(6)\,\mathrm{s}^{-1}$ (5.58(13)% modulation) and the 2014 June observation has rms amplitude $0.233(6)\,\mathrm{s}^{-1}$ (5.81(14)%). Second panel: the difference between the scaled LMXB-state profiles. Third panel: the X-ray pulse profile observed during the 2008 November observation reported in Archibald et al. (2010), during which PSR J1023+0038 was in the RMSP state (RMS amplitude $0.0099(18)\,s^{-1}$, 8.8(1.6)%). Bottom panel: the difference between the LMXB-state profile (from 2014 June) and a suitably scaled version of that observed during the RMSP state (in 2008 November).

and 2014 June observations.

The majority of the photons were collected during the high mode, where we find that the 0.3–10 keV X-rays are pulsed with a root-mean-square pulsed fraction of 8.13(14)% (count rate $0.311(5)\,\mathrm{s}^{-1}$; see also Figure 4). In the low mode we detect no significant pulsations, and set a 95% confidence upper limit on the pulsed fraction of 2.4% (count rate $0.016\,\mathrm{s}^{-1}$). This implies that if any pulsations are present in the low mode, they must form a substantially smaller luminosity fraction (and much smaller absolute luminosity) in the low mode than they do in the high mode. Pulsations are also not detected during the flares, with a 95% upper limit on the pulsed fraction of 1.4% (count rate $0.15\,\mathrm{s}^{-1}$): if any pulsations are present during the flares, they must be weaker in absolute luminosity than during the high mode. In other words, the flares are not simply the addition of unmodulated emission to the high mode; the pulsations appear to be suppressed during flares.

4. DISCUSSION

The detection of X-ray pulsations strongly suggests that PSR J1023+0038 undergoes channeled accretion onto the stellar surface (at the magnetic poles) but at an X-ray luminosity of $3 \times 10^{33}\,\mathrm{erg\,s}^{-1}$ — a level that is considered quiescent for normal LMXBs, and which is close to two orders of magnitude less than the luminosities at which AMXPs have previously been seen to pulsate ($\gtrsim 10^{35}\,\mathrm{erg\,s}^{-1}$; see Figure 5 and Table 1). The observed pulse profile shapes in AMXPs are a consequence of the hot spots on the surface of the rotating star or shocks barely above it. PSR J1023+0038's pulsation characteristics are strikingly similar to other, higher-luminosity AMXPs: namely, a low pulsed fraction, roughly sinusoidal pulse shape, and a fairly hard spectrum (Patruno & Watts 2012). The large duty cycle of the high-luminosity mode (∼70%), the only one to exhibit X-ray pulsations, suggests that the channeled accretion flow in PSR J1023+0038 is able to reach the magnetic polar caps on the stellar surface the majority of the time, but with frequent, short interruptions.

This unusual combination of phenomena appears not to be unique. While this paper was in the refereeing process, Papitto et al. (2014) reported the discovery of coherent X-ray pulsations from another transitioning RMSP, XSS J12270−4859, with very similar behaviour: presence in the high but not low or flare modes, system X-ray luminosity of 10^{33}–$10^{34}\,\mathrm{erg\,s}^{-1}$, double-peaked profile, and pulsed fraction of 7.7(5)%.

Theoretical models of accretion onto a magnetized neutron star must therefore account for the entirety of the rich phenomenology of PSR J1023+0038 and XSS J12270−4859: the rapid, stochastic switching between the three discrete luminosity modes — low, high, and flare — two of which maintain a fairly narrow range of luminosities on time scales ranging from minutes to several hours (and are also remarkably similar between observations separated by 7 months), and only one of which permits detectable X-ray pulsations.

The simplest model for accretion regulated by a stellar magnetic field assumes that a geometrically thin disk is truncated at the 'magnetospheric radius', where the ram pressure of the gas balances the pressure of the magnetic field (Pringle & Rees 1972): $r_\mathrm{m} \simeq (B_*R_*^3)^{4/7}(GM_*/2)^{1/7}\dot{M}^{-2/7}$. This radius is compared with the 'co-rotation radius' ($r_\mathrm{c} \equiv GM_*/\Omega_*^2 = 24\,\mathrm{km}$ for PSR J1023+0038), the location where the orbital velocity matches the star's spin. When $r_\mathrm{m} > r_\mathrm{c}$, the star spins faster than the flow and inhibits accretion, instead expelling incoming gas from the system (the 'propeller' regime; Illarionov & Sunyaev 1975). For PSR J1023+0038, the transition to the propeller regime occurs at $\sim 5 \times 10^{-10}\ M_\odot\ \mathrm{yr}^{-1}$ and $8 \times 10^{35}\ \mathrm{erg\ s}^{-1}$ — substantially higher than the luminosity of PSR J1023+0038 in its high-luminosity mode. For comparison, assuming the entire high mode X-ray flux comes from accretion onto the star's surface, we obtain a mass flow rate of $9 \times 10^{-13}\ M_\odot\ \mathrm{yr}^{-1}$, almost three orders of magnitude lower and only $\sim 10^{-4}$ of the Eddington accretion rate. Even the highest plausible high-mode bolometric luminosity, $10^{35}\,\mathrm{erg\,s}^{-1}$, corresponds to only $10^{-11}\,M_\odot\,\mathrm{yr}^{-1}$, still insufficient to permit accretion onto the surface in this model.

Our detection of pulsations at quiescent luminosities shows that the simple accretion/propeller picture is incomplete. There are several possible theoretical resolu-

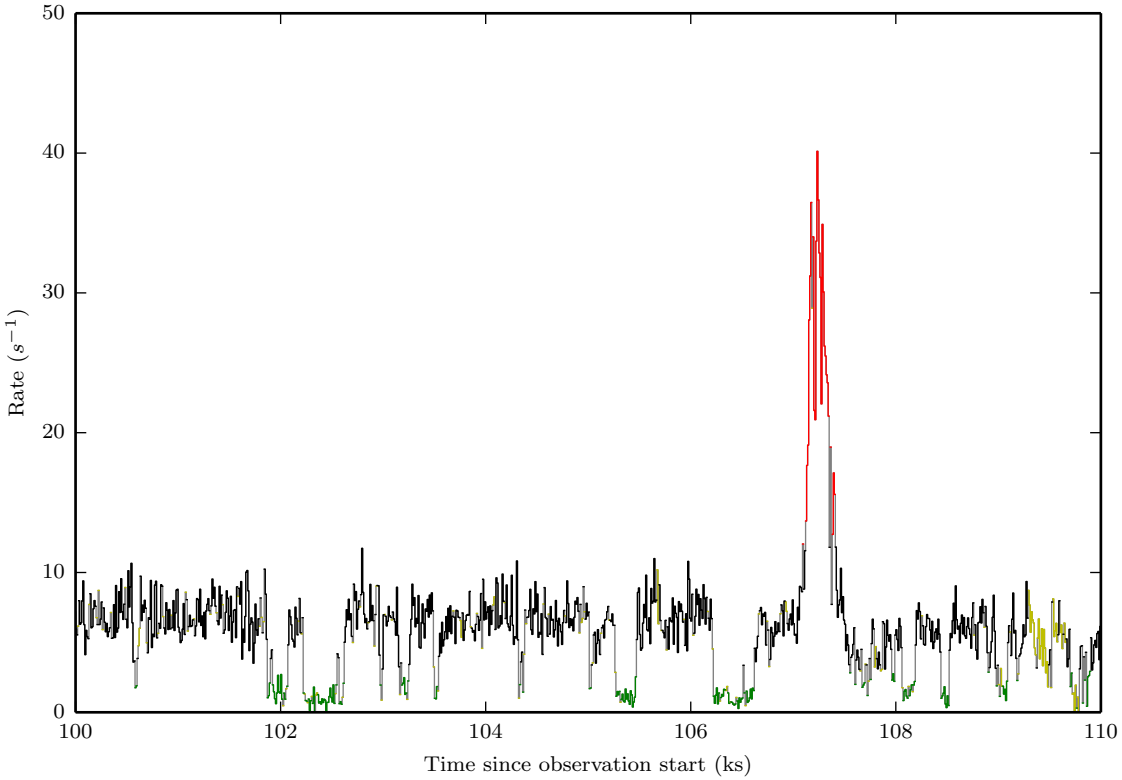

Figure 3. A short section of the combined *XMM-Newton* light-curve, showing the low (green), high (black), and flare (red) modes. Times at which the mode is indeterminate are marked in grey, and times excluded from pulsation searching because of background flaring are marked in yellow. See Figure A1 for how the thresholds were set, and Figure A2 for the whole light curve.

tions, each of which suggests intriguing new insights for accretion physics at low luminosities. The first is that the inner accretion flow could be 'radiatively inefficient', meaning that the accretion flow changes from an optically thick disk to an optically thin, geometrically thick disk (Rees et al. 1982) and most of the accretion energy goes into the kinetic energy of ejected material rather than being radiated away (so the accretion rate is much higher than the luminosity would suggest). In this case the accretion rate could be high enough to put $r_{\rm m}$ near $r_{\rm c}$, so that in the high mode some small fraction of the material can accrete onto the star. Alternately, the coupling between magnetic field lines and the highly conducting accretion flow may not be efficient. This can lead to diffusion of gas inward via Rayleigh-Taylor instabilities (Kulkarni & Romanova 2008), or a large-scale compression of the magnetic field, both of which have been seen in numerical simulations (Romanova et al. 2005; Ustyugova et al. 2006; Zanni & Ferreira 2013). As a result, although the naively-computed magnetospheric radius remains well outside the corotation radius, a fraction of the gas is nevertheless able to overcome the magnetic field's centrifugal barrier and accrete onto the star.

Finally, a propeller may not form at all. Propeller-mode accretion can only eject infalling material if the magnetic field at $r_{\rm m}$ rotates significantly faster than the disk, which occurs well beyond the co-rotation radius (Spruit & Taam 1993). If this is not the case, gas stays confined in the inner part of the flow, and $r_{\rm m}$ is 'trapped' near corotation (D'Angelo & Spruit 2010, 2012; Siuniaev & Shakura 1977). The gas flow serves as a large reservoir of matter whose mass provides the inward pressure to balance the magnetic stress and results also in accretion episodes in spite of a low net accretion rate. The switching between low and high mode might be the result of transitions between a non-accreting pure propeller mode and an accreting trapped-disk mode.

While the high-mode luminosity provides a bound on how much matter reaches the neutron star, it is more difficult to measure the amount of material flowing into the inner regions if some of this matter is ejected. Our radio continuum observations have detected a flat-spectrum radio source, which is strong evidence for an outflow, and which may be driven either by a strong propeller (Romanova et al. 2005; Ustyugova et al. 2006; Zanni & Ferreira 2013) or by the intrinsic accretion flow properties (as in black holes). Further modeling is required to see whether propeller-mode accretion can, with minimal radiation, eject the vast majority of the inflowing material, leaving less than 1% to fall on the neutron-star surface. For comparison, the accreting white dwarf AE Aquarii, considered to be the clearest example of propeller-mode accretion, appears to be allowing only 0.3% of the incoming material to reach the surface, but on the other hand most of the soft X-ray luminosity is produced in the inflow before ejection or accretion onto the surface (Oruru & Meintjes 2012).

PSR J1023+0038 likely still has more to offer in the quest to unravel the true nature of low-level accretion onto neutron stars; in particular, continued observations yielding a measurement of the change in spin-down rate caused by this current episode will be crucial in revealing

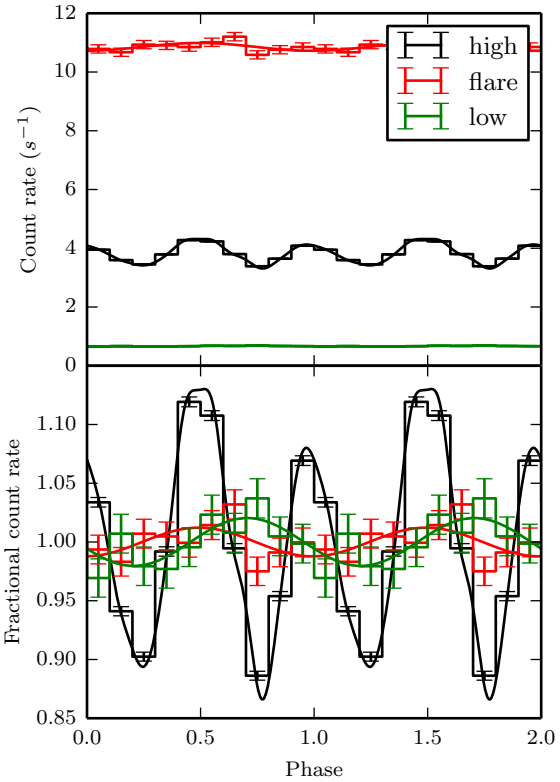

Figure 4. X-ray pulse profiles during the low, high, and flare modes. Each contains background-subtracted combined data from both 2013 November and 2014 June observations. The top panel shows all three normalized by count rate, while the bottom panel shows all three normalized to the same mean value. In the low mode, pulsations are not detected: the H test reports a false positive probability of 0.2; a 95% confidence upper limit on the plausible pulsed fraction is about 2.4% (that is, if the pulsed fraction were 2.4% we would obtain a false positive probability smaller than this 95% of the time). This corresponds to a maximum possible pulsed flux in the low mode of $0.016\,\mathrm{s}^{-1}$. In the high mode, the pulsed flux (fraction) is $0.311(5)\,\mathrm{s}^{-1}$ (8.13(14)%). In the flare mode we also do not detect pulsations with a false positive probability of 0.2, giving an upper limit on the pulsed fraction of 1.4% and the pulsed flux of $0.15\,\mathrm{s}^{-1}$; note that this 95% upper limit on the pulsed flux is *less* than the pulsed flux during the high mode.

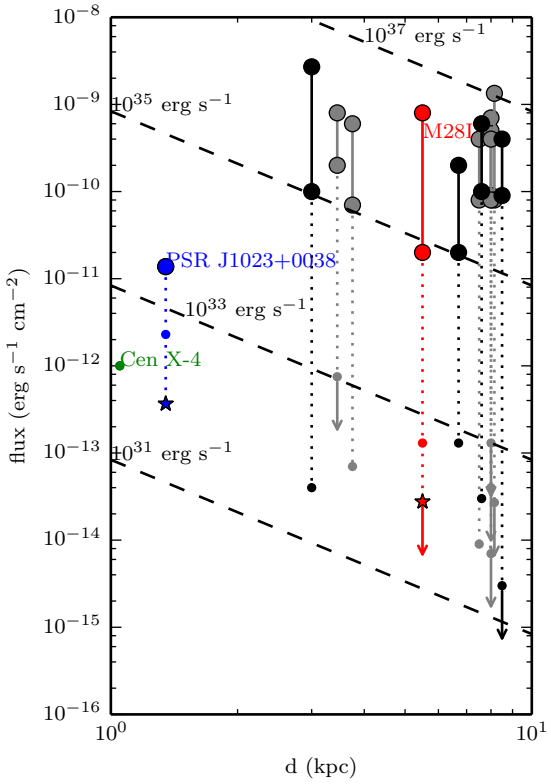

Figure 5. Approximate X-ray fluxes of AMXPs. Large circles connected by solid lines indicate the range of fluxes at which coherent X-ray pulsations have been detected, while dotted lines and small circles indicate the range of quiescent flux levels (arrows indicate where only an upper limit on quiescent flux is available). Stars indicate X-ray fluxes during a RMSP state. The horizontal axis is distance, generally the largest uncertainty, and the dashed diagonal lines show constant luminosities. Marked in red is the transition system PSR J1824−2452I (also called M28I), and in blue is PSR J1023+0038 (in both cases the distances are well known). For PSR J1023+0038, the large circle shows the high-state flux (where pulsations were detected) and the small circle shows low-state flux (where no pulsations were detected). Cen X-4 is marked in green. AMXPs with relatively good distance estimates are marked in black, whereas those where the distance is more uncertain are marked in grey. For details and references see Table 1.

the ratio between accreted and ejected material.

The results presented were based on observations obtained with *XMM-Newton*, an ESA science mission with instruments and contributions directly funded by ESA Member States and NASA. The National Radio Astronomy Observatory is a facility of the National Science Foundation operated under cooperative agreement by Associated Universities, Inc. A.M.A. was funded for this work through an NWO Vrije Competitie grant to J.W.T.H.. A.P. acknowledges support from an NWO Vidi fellowship. J.W.T.H. and C.B. further acknowledge funding from an NWO Vidi fellowship and ERC Starting Grant 'DRAGNET' (337062; PI J.W.T.H.). A.T.D. acknowledges support from an NWO Veni Fellowship. V.M.K. acknowledges support from an NSERC Discovery Grant and Accelerator Supplement, the FQRNT Centre de Recherche Astrophysique du Québec, an R. Howard Webster Foundation Fellowship from the Canadian Institute for Advanced Research (CIFAR), the Canada Research Chairs Program and the Lorne Trottier Chair in Astrophysics and Cosmology.

Facilities: XMM VLA

APPENDIX

PULSED FLUXES AND FRACTIONS.

The H test is an effective tool for detecting the presence of pulsations, but we would often like to quantify the pulsations in order to describe the degree of modulation of the X-ray flux. The obvious approach is to choose the minimum of the light curve as an estimate of the constant background flux and then give the fraction of photons above that minimum as the pulsed fraction. Unfortunately this suffers from a potentially serious statistical bias: the process of choosing the minimum of a noisy light curve unavoidably tends to underestimate the minimum of the true light curve. The uncertainty on the pulsed fraction is also large, since it is set by the uncertainty on the minimum of the light curve. We therefore use another way to describe the pulsed flux: we report the root-mean-squared modulation. If the true light

Table 1
AMXP flux ranges and distances

Name	d (kpc)	Observed pulsation flux (10^{-10}erg s^{-1} cm^{-2})	Quiescent flux (10^{-14}erg s^{-1} cm^{-2})	Refs.
PSR J1023+0038	1.4	0.14 [a]	229.3 [a]	**This work**
Cen X-4	0.9–1.2 (?)	...	100.0 [b]	(1)
IGR J00291+5934	2.5–5.0 (?)	0.70 – 6.00 [c]	7.0 [b]	(2),(3)
IGR J17498-2921	7.6	1.00 – 6.00 [d]	3.0 [b]	(4),(5)
IGR J17511-3507	< 6.9 (?)	2.00 – 8.00 [e]	< 75.0 [b]	(6),(7)
PSR J1824-2452I (M28I)	5.5	0.20 – 8.00 [b]	13.0 [f]	(8),(9)
NGC6440 X-2	8.1–8.9	0.90 – 4.00 [g]	< 0.3 [b]	(10),(11)
SAX J1808.4-3658	2.5–3.5	1.00 – 27.00 [e]	4.0 [b]	(12),(3)
Swift J1749.4-2807	5.4–8.0	0.20 – 2.00 [g]	13.0 [b]	(13),(5)
Swift J1756.9-2508	8.0 (?)	0.80 – 4.00 [h]	< 13.0 [f]	(14),(15)
XTE J0929-314	> 5.0 (?)	0.80 – 4.00 [d]	0.9 [b]	(16),(17)
XTE J1751-305	> 6.3 (?)	0.80 – 13.40 [d]	< 2.7 [b]	(18),(17)
XTE J1807-294	8.0 (?)	0.90 – 7.00 [d]	< 4.0 [b]	(19),(20)
XTE J1814-338	8.0 (?)	0.90 – 5.00 [e]	< 0.7 [b]	(21),(3)

Note. — AMXP parameters used in Figure 5. Distances with a question mark indicate distance estimates highly dependent on assumptions. Energy ranges are indicated by superscript letters: *a*: 0.3 – 10.0, *b*: 0.5 – 10.0, *c*: 2.5 – 25.0, *d*: 2.0 – 10.0, *e*: 2.0 – 25.0, *f*: 0.3 – 8.0, *g*: 2.0 – 16.0, and *h*: 2.5 – 16.0 keV. No pulsations have been detected from Cen X-4, so it is not an AMXP; it is included because accretion onto the surface has been detected. References: (1) Cackett et al. (2013), (2) Hartman et al. (2011), (3) Heinke et al. (2009), (4) Papitto et al. (2011), (5) Degenaar et al. (2012), (6) Riggio et al. (2011b), (7) Haskell et al. (2012), (8) Ferrigno et al. (2014), (9) Linares et al. (2014), (10) Patruno & D'Angelo (2013), (11) Heinke et al. (2010), (12) Hartman et al. (2008), (13) Altamirano et al. (2011), (14) Patruno et al. (2010), (15) Papitto et al. (2007), (16) Galloway et al. (2002), (17) Wijnands et al. (2005), (18) Riggio et al. (2011a), (19) Riggio et al. (2008), (20) Campana et al. (2005), (21) Haskell & Patruno (2011)

curve is $f(\phi)$, we report

$$F_{rms} = \int (f(\phi) - \bar{f})^2 d\phi,$$

where $\bar{f}$ is the mean of $f(\phi)$. The relationship between this and the above definition is a scaling that depends on the pulse profile shape.

The rms pulsed flux can be reliably estimated from the Fourier coefficients of the profile using Parseval's theorem, with correction terms to reduce the bias, as

$$F^2_{rms} = \sum_{j=1}^{m} a_j^2 + b_j^2 - \sigma^2_{a,j} - \sigma^2_{b,j},$$

where a_j and b_j are the jth Fourier coefficient, $\sigma_{a,j}$ and $\sigma_{b,j}$ are their uncertainties, and m is a suitable number of harmonics. If a_j and b_j are normally distributed around the true values, then an easy computation shows that the expected value of F^2_{rms} is the true rms pulsed flux; in other words this is an unbiased estimator. Unfortunately taking the square root introduces a small amount of bias, and in fact since F^2_{rms} can turn out to be negative one must report zero in some cases, but this provides a way of computing the pulsed flux that has low uncertainty and little bias.

A priori m can be chosen freely without biasing the result, but too small an m will distort the estimated profile by failing to include real structure, while too large an m will distort the estimated profile by including Fourier coefficients dominated by noise. There is a simple criterion for choosing m: select the value m that maximizes $\left(\sum_{j=1}^{m}(a_j/\sigma_{a,j})^2 + (b_j/\sigma_{b,j})^2\right) - 4m$. This criterion asymptotically selects the m that minimizes the expected mean integrated squared error between the estimated profile and the true profile (de Jager et al. 1986). This is also the value of m used in the H test, and it is suitable for graphical profile representations as well as choice-free pulsed flux estimation.

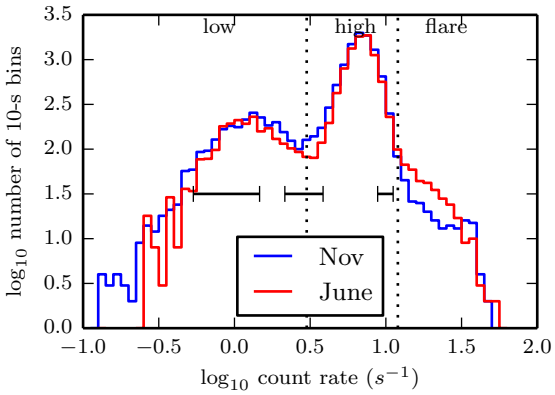

Figure A1. Distribution of fluxes in the 2013 November and 2014 June observations. All pn and MOS photons from both observations were combined to form an exposure-corrected light curve with 10-second time bins, and histograms of the resulting count rates are plotted. Horizontal error bars show the horizontal smearing due to Poisson noise in the light curve bins. Vertical dotted lines show the cuts we chose between low, high, and flare modes.

To construct the smooth profile approxmations in Figures 2 and 4, we computed the empirical Fourier coefficients of the set of photon phases ($A_m = \sum_k e^{2\pi i m \phi_k}$), truncated them at the value of m obtained from the above procedure, and plotted the resulting curve.

PROFILE COMPARISON.

For the purposes of comparing the X-ray profiles between our two LMXB-state observations and to the RMSP-state X-ray profile, we formed profiles using the above optimal numbers of harmonics and aligned all three using cross-correlation. To form the difference profiles in Figure 2 we also scaled and offset one of the profiles to the least-squares best-fit values. We formed the

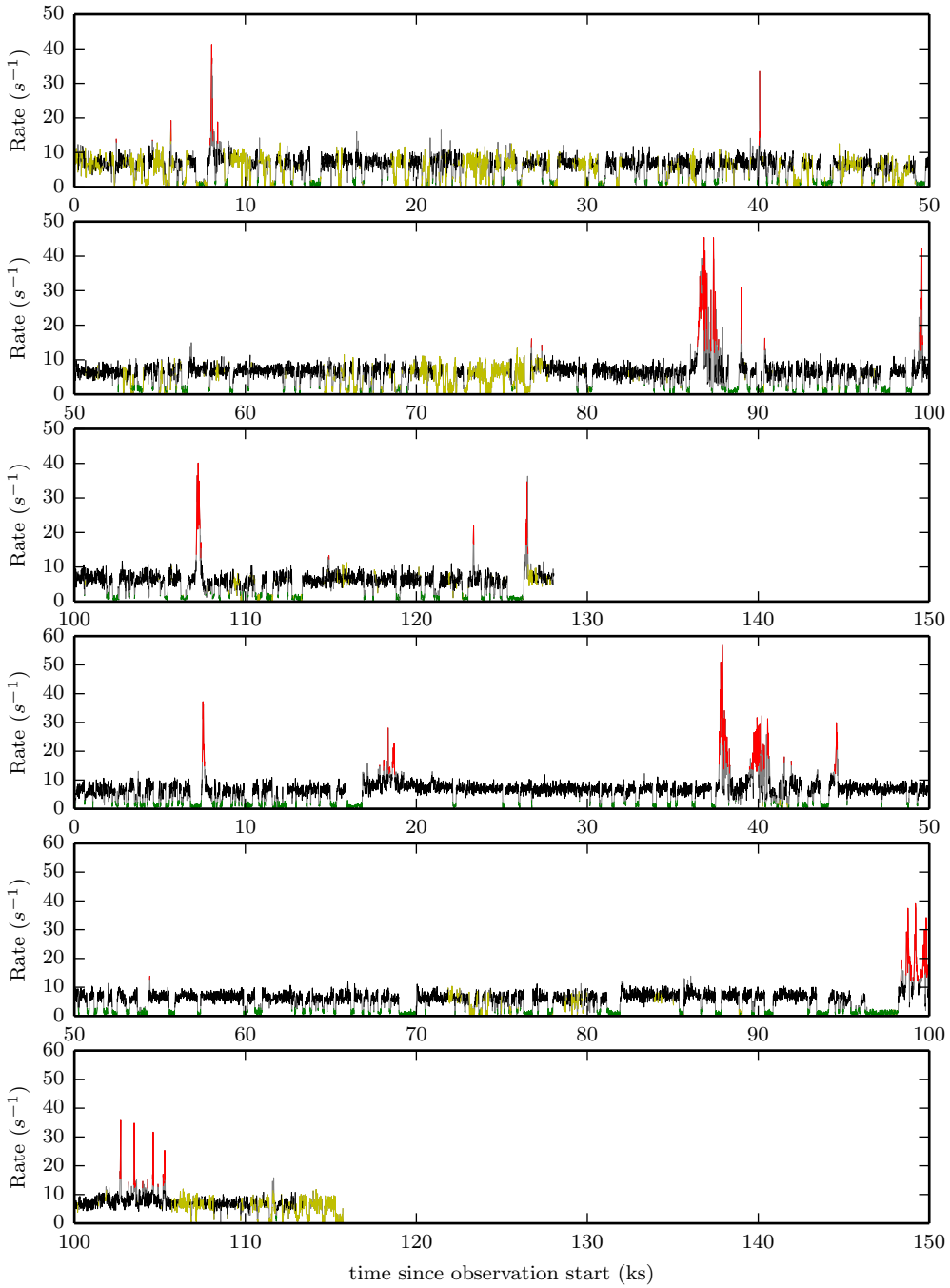

Figure A2. Combined X-ray light curve showing classification of times into low, high, flare, ambiguous, or background flaring. This light curve is formed using exposure-corrected and background-subtracted data from the pn and both MOS cameras in 10-s time bins. Regions marked in green are classified as low-mode, black as high-mode, and red as flares; the gray regions were treated as ambiguous, and the yellow regions suffered from background flaring, and neither were used in pulsation searches. The top three panels of this light curve are from the 2013 November observation, while the bottom three are from the 2014 June observation.

smoothed profiles in Figure 4 using the same Fourier-domain approach.

REFERENCES

Altamirano, D., Cavecchi, Y., Patruno, A., et al. 2011, ApJ, 727, L18
Archibald, A. M., Kaspi, V. M., Bogdanov, S., et al. 2010, ApJ, 722, 88
Archibald, A. M., Kaspi, V. M., Hessels, J. W. T., et al. 2013, ArXiv e-prints 1311.5161, arXiv:1311.5161
Archibald, A. M., Stairs, I. H., Ransom, S. M., et al. 2009, Science, 324, 1411
Bogdanov, S., Archibald, A. M., Bassa, C., et al. 2014, ArXiv e-prints, arXiv:1412.5145
Cackett, E. M., Brown, E. F., Degenaar, N., et al. 2013, MNRAS, 433, 1362
Campana, S., Colpi, M., Mereghetti, S., Stella, L., & Tavani, M. 1998, A&A Rev., 8, 279
Campana, S., Ferrari, N., Stella, L., & Israel, G. L. 2005, A&A, 434, L9
Coti Zelati, F., Baglio, M. C., Campana, S., et al. 2014, MNRAS, 444, 1783
D'Angelo, C. R., Fridriksson, J. K., Messenger, C., & Patruno, A. 2015, MNRAS, 449, 2803
D'Angelo, C. R., & Spruit, H. C. 2010, MNRAS, 406, 1208
—. 2012, MNRAS, 420, 416
de Jager, O. C., Raubenheimer, B. C., & Swanepoel, J. W. H. 1986, A&A, 170, 187
—. 1989, A&A, 221, 180
de Martino, D., Belloni, T., Falanga, M., et al. 2013, A&A, 550, A89
Degenaar, N., Patruno, A., & Wijnands, R. 2012, ApJ, 756, 148
Deller, A. T., Archibald, A. M., Brisken, W. F., et al. 2012, ApJ, 756, L25
Deller, A. T., Moldón, J., Miller-Jones, J. C. A., et al. 2014, ArXiv e-prints, arXiv:1412.5155
Ferrigno, C., Bozzo, E., Papitto, A., et al. 2014, A&A, 567, A77
Galloway, D. K., Chakrabarty, D., Morgan, E. H., & Remillard, R. A. 2002, ApJ, 576, L137
Halpern, J. P., Gaidos, E., Sheffield, A., Price-Whelan, A. M., & Bogdanov, S. 2013, The Astronomer's Telegram, 5514, 1
Hartman, J. M., Galloway, D. K., & Chakrabarty, D. 2011, ApJ, 726, 26
Hartman, J. M., Patruno, A., Chakrabarty, D., et al. 2008, ApJ, 675, 1468
Haskell, B., Degenaar, N., & Ho, W. C. G. 2012, MNRAS, 424, 93
Haskell, B., & Patruno, A. 2011, ApJ, 738, L14
Heinke, C. O., Jonker, P. G., Wijnands, R., Deloye, C. J., & Taam, R. E. 2009, ApJ, 691, 1035
Heinke, C. O., Altamirano, D., Cohn, H. N., et al. 2010, ApJ, 714, 894
Illarionov, A. F., & Sunyaev, R. A. 1975, A&A, 39, 185
Kulkarni, A. K., & Romanova, M. M. 2008, MNRAS, 386, 673
Linares, M. 2014, ApJ, 795, 72
Linares, M., Bahramian, A., Heinke, C., et al. 2014, MNRAS, 438, 251
Martin-Carrillo, A., Kirsch, M. G. F., Caballero, I., et al. 2012, A&A, 545, A126
McMullin, J. P., Waters, B., Schiebel, D., Young, W., & Golap, K. 2007, in Astronomical Society of the Pacific Conference Series, Vol. 376, Astronomical Data Analysis Software and Systems XVI, ed. R. A. Shaw, F. Hill, & D. J. Bell, 127
Migliari, S., & Fender, R. P. 2006, MNRAS, 366, 79
Oruru, B., & Meintjes, P. J. 2012, MNRAS, 421, 1557
Papitto, A., de Martino, D., Belloni, T. M., et al. 2014, ArXiv e-prints, arXiv:1412.4252
Papitto, A., di Salvo, T., Burderi, L., et al. 2007, The Astronomer's Telegram, 1133, 1
Papitto, A., Bozzo, E., Ferrigno, C., et al. 2011, A&A, 535, L4
Patruno, A., Altamirano, D., & Messenger, C. 2010, MNRAS, 403, 1426
Patruno, A., & D'Angelo, C. 2013, ApJ, 771, 94
Patruno, A., & Watts, A. L. 2012, ArXiv e-prints 1206.2727, arXiv:1206.2727
Patruno, A., Archibald, A. M., Hessels, J. W. T., et al. 2014, ApJ, 781, L3
Pringle, J. E., & Rees, M. J. 1972, A&A, 21, 1
Rees, M. J., Begelman, M. C., Blandford, R. D., & Phinney, E. S. 1982, Nature, 295, 17
Riggio, A., Burderi, L., di Salvo, T., et al. 2011a, A&A, 531, A140
Riggio, A., Di Salvo, T., Burderi, L., et al. 2008, ApJ, 678, 1273
Riggio, A., Papitto, A., Burderi, L., et al. 2011b, A&A, 526, A95
Romanova, M. M., Ustyugova, G. V., Koldoba, A. V., & Lovelace, R. V. E. 2005, ApJ, 635, L165
Siuniaev, R. A., & Shakura, N. I. 1977, Pisma v Astronomicheskii Zhurnal, 3, 262
Spruit, H. C., & Taam, R. E. 1993, ApJ, 402, 593
Stappers, B. W., Archibald, A. M., Hessels, J. W. T., et al. 2014, ApJ, 790, 39
Strohmayer, T., & Bildsten, L. 2006, New views of thermonuclear bursts, ed. W. H. G. Lewin & M. van der Klis, 113–156
Tendulkar, S. P., Yang, C., An, H., et al. 2014, ApJ, 791, 77
Thorstensen, J. R., & Armstrong, E. 2005, AJ, 130, 759
Ustyugova, G. V., Koldoba, A. V., Romanova, M. M., & Lovelace, R. V. E. 2006, ApJ, 646, 304
Wijnands, R., Homan, J., Heinke, C. O., Miller, J. M., & Lewin, W. H. G. 2005, ApJ, 619, 492
Zanni, C., & Ferreira, J. 2013, A&A, 550, A99